A new wave height distribution for intermediate and shallow water depths

I. Karmpadakis [*], C. Swan, M. Christou

Department of Civil & Environmental Engineering, Imperial College London, SW7 2AZ, UK

ARTICLE INFO

ABSTRACT

The present paper addresses the short-term distribution of zero-crossing wave heights in intermediate and shallow water depths. New physical insights are provided regarding the effects of nonlinearity, directionality, reduced effective water depth and finite spectral bandwidth. These are demonstrated through the analysis of a large database of experimental simulations of short-crested sea-states on flat bed bathymetries. A new wave height model is proposed building upon these physical insights and is calibrated using the experimental data. Independent comparisons between field measurements and the proposed model indicate that it is appropriate to a wide range of incident wave conditions and that it provides considerable improvement over existing models.

1. Introduction

The distribution of (zero-crossing) wave heights represents one of the most important inputs for a very wide range of applications in coastal and marine engineering. Examples of such applications include the estimation of wave loading on coastal structures (Goda, 2010), the calculation of wave overtopping (Van der Meer et al., 2018) and the design of offshore structures and wind turbines (DNV, 2010).

In many cases, representative wave heights, such as the largest one-tenth wave height ($H_{1/10}$), are derived directly from a suitable distribution and used as input to design calculations. In other cases, individual wave heights or the complete distribution are assumed at an offshore location and propagated towards the shoreline using numerical models and transformation techniques. As such, errors in the estimation of the wave height distribution can easily propagate throughout the design process generating additional uncertainty and inaccuracies in calculations.

Despite the abundance of methods to describe the distribution of wave heights, a number of issues have been raised and have not been fully resolved. For example, Karmpadakis et al. (2020) presented an assessment of the most widely applied statistical distributions using a large database of field measurements in intermediate and shallow water depths. This study indicated that none of the available models is capable of predicting wave heights across the broad range of environmental conditions encountered over flat beds. Building upon these results, the present paper proposes a new wave height distribution, which is shown to provide an improvement over existing methods.

More specifically, this paper provides an analysis of experimental measurements undertaken in two laboratory facilities, covering a broad range of incident wave conditions and water depths. The purpose of these experiments is to shed light on the main physical mechanisms that drive the distribution of wave heights. These insights are then used to derive a new wave height distribution. The proposed distribution is validated against field data recorded by wave radars in intermediate and shallow water depth locations in the southern North Sea.

The contents of this paper are arranged as follows. First, a brief overview of literature relevant to the distribution of wave heights is given in Section 2. Then, the characteristics of the experimental and field measurements are presented in Section 3. Section 4 provides the fundamental physical insights arising from the analysis of the laboratory measurements, while Section 5 presents the development of the new wave height distribution. Section 6 provides comparisons to available field data and finally, the key conclusions arising from the present study are provided in Section 7.

2. Background

The distribution of wave heights has received considerable attention in both the literature and engineering practice. Relevant research can be sub-divided into two categories based on the water depth regime. In both deep and shallow water depths, the Rayleigh distribution (Longuet-Higgins, 1952) has largely been adopted as a reference model or an initial approximation. However, it has long been established that the Rayleigh distribution over-predicts the largest waves in realistic sea-states (Longuet-Higgins, 1980; Forristall, 1984; Tayfun, 1990; Battjes and Groenendijk, 2000; Goda, 2010).

In deep water, several models seek to account for this over-prediction by incorporating finite spectral bandwidth effects (Tayfun, 1981; Naess, 1985; Boccotti, 1989; Tayfun, 1990). These models are based upon linear wave theory and have been extensively assessed using numerical, experimental and field measurements in deep water (Tayfun and Fedele, 2007; Casas-Prat and Holthuijsen, 2010). The largest wave heights predicted by the Naess (1985) model are slightly lower than the asymptotic models of Boccotti (1989) and Tayfun (1990), which are generally in good mutual agreement (Tayfun and Fedele, 2007).

Effects arising at a second-order of wave steepness tend to increase the elevations of both wave crests and troughs by a comparable amount. As a result, wave heights remain largely unaffected by the incorporation of second-order corrections (Longuet-Higgins and Stewart, 1960; Sharma and Dean, 1981; Fedele and Arena, 2005). In fact, Tayfun and Fedele (2007) find that discrepancies between linear and second-order predictions are less than 2% for the largest waves. In contrast, higher-order nonlinear effects have been shown to affect the distribution of wave heights in deep water under some conditions. These typically relate to resonant interactions arising in narrow-banded, unidirectional sea-states. Based on the Gram–Charlier series expansion, Mori and Janssen (2006) and Tayfun and Fedele (2007) have proposed models that can describe these increases. More recently, Alkhalidi and Tayfun (2013) combined the Boccotti and Gram–Charlier models to produce a flexible, asymptotic distribution that accounts for both finite bandwidth and third-order nonlinearities. The Generalised Boccotti distribution has been shown to perform well against experimental and field measurements. Finally, Forristall (1978) calibrated a Weibull distribution to field measurements and produced a model that has been extensively used in industry for both deep and intermediate water depths.

As the water depth reduces, the main focus of wave height models shifts to incorporate the effects of wave breaking. This is generally achieved by empirically calibrating models to unidirectional laboratory experiments on sloping bathymetries. Glukhovskiy (1966) parametrised a distribution that uses the ratio of the mean wave height over the water depth, H_m/d, to incorporate energy dissipation in the largest waves due to wave breaking. Since H_m is not a quantity that is known *a priori*, van Vledder (1991) and Klopman (1996) provided alternative parametrisations that allow the Glukhovskiy distribution to be used in a predictive manner. Recently, Karmpadakis et al. (2020) found good agreement between the Glukhovskiy-type models and field measurements for sea-states that incorporate relatively limited wave breaking.

Battjes and Groenendijk (2000) observed that experimentally generated wave heights are governed by different distributions based on whether they are breaking or not. They proposed a split structure distribution which includes a Rayleigh distribution for lower wave heights and a parametrised Weibull form for the largest waves. The empirical coefficients of this model have been derived on the basis of unidirectional flume experiments on sloping beds of varying gradient. Despite the wide adoption of the Battjes and Groenendijk (2000) model, subsequent studies suggest that alternative empirical coefficients would be more effective with respect to some datasets (Mai et al., 2011; Caires and Van Gent, 2012). Along similar lines, Wu et al. (2016) propose a different split structure model which uses a Weibull distribution for the main body of the distribution and a Generalised Pareto distribution for the tail. Finally, Mendez et al. (2004) employed a wave energy propagation model to account for linear shoaling and wave breaking. The proposed model was shown to have similar accuracy as the Battjes and Groenendijk (2000) model for experimental data on sloping beds.

Taken together, the state-of-the-art regarding wave height distributions includes a variety of conceptually different models. Recent reviews by Tayfun and Fedele (2007), Casas-Prat and Holthuijsen (2010) and Karmpadakis et al. (2020) indicate that each of these models are successful in at least one water depth regime. However, no single

Table 1
Definition of the laboratory test cases in the Imperial College London (ICL) wave basin with $d = 50$ m.

Sea-state	T_p [s]	H_s [m]	S_p [–]	σ_θ [°]	$k_p d$ [–]
IA1		2.2	0.01		
IA2		4.4	0.02		
IA3		6.7	0.03		
IA4	12	8.9	0.04	10, 20	1.53
IA5		11.2	0.05		
IA6		13.4	0.06		
IA7		15.7	0.07		
IB1		3.0	0.01		
IB2		6.1	0.02		
IB3	14	9.1	0.03	10, 20	1.22
IB4		12.2	0.04		
IB5		15.3	0.05		
IB6		18.3	0.06		
IC1		4.0	0.01		
IC2		8.0	0.02		
IC3	16	12.0	0.03	10, 20	1.02
IC4		16.0	0.04		
IC5		20.0	0.05		

distribution is capable of describing wave heights in a broader range of conditions (Karmpadakis et al., 2020). In deep water, the models of Boccotti (1989) and Tayfun (1990) compare well with measured data, but are not formulated to incorporate wave breaking. At the same time, there is little observational evidence that higher-order nonlinear corrections (due to, for example, modulational instabilities) are important in realistic sea-states (Fedele et al., 2016, 2019). In shallow water, all wave height distributions have been calibrated with unidirectional experimental data generated on sloping beds. As such, wave heights arising in steep, broad-banded and short-crested sea-states over flat beds are not generally considered.

3. Methodology

To address these outstanding questions, two methods of analysis have been employed. First, laboratory measurements are used to provide insights into the dominant physical mechanisms controlling the wave height distribution. These insights provide the basis for the new wave height model. Second, surface elevation measurements from a number of locations in the North Sea are utilised to validate the accuracy of the proposed model.

The experimental data have been generated in two directional wave basins with very different operational characteristics; one located at Imperial College London (ICL) and the other at Queen's University Belfast (QUB). The ICL wave basin has plan dimensions of 10 m x 20 m, a water depth of $d = 0.5$ m and 56 bottom-hinged, flap-type wave paddles mounted along its long side. In contrast, the QUB wave basin has plan dimensions of 18 m x 16 m with 24 piston-type wave paddles mounted along a short side. This facility consists of a flat bed region followed by a combination of mild slopes; the water depth is adjustable and varied between $d = 0.6$ m, 0.5 m and 0.4 m in the flat bed region. In both facilities wave generation and active wave absorption were based upon force-feedback control (Spinneken and Swan, 2012) and were coupled with efficient passive absorbing beaches at the downstream end. With this combination reflection coefficients were less than 5% for all generated wave frequencies.

Water surface elevations were measured using resistive-type wave gauges with a sampling rate of $f_s = 128$ Hz. This is sufficiently large to resolve high-frequency effects and avoid the need for post-processing. In both facilities arrays of wave gauges were deployed and analysed; the aim being to verify the correct operation of the apparatus. However, in the present study only wave measurements recorded at the centre of the flat bed regions are presented, unless otherwise mentioned.

Table 2

Definition of the laboratory test cases in the Queen's University Belfast (QUB) wave basin.

Sea-state	T_p [s]	H_s [m]	S_p [–]	σ_θ [°]	d [m]
Q1A5-10	12	12	0.053	10	
Q1B2-10	14	6.1	0.02	10	
Q1B2-20	14	6.1	0.02	20	
Q1B3-10	14	9.1	0.03	10	60
Q1B3-20	14	9.1	0.03	20	
Q1B4-10	14	12.2	0.04	10	
Q1B5-10	14	15.3	0.05	20	
Q2A2-10	12	4.4	0.02	10	50
Q3B2-10	14	6.1	0.02	10	
Q3B2-20	14	6.1	0.02	20	
Q3B3-10	14	9.1	0.02	10	40
Q3B3-20	14	9.1	0.02	20	
Q3C2-10	16	8.0	0.02	10	
Q3D2-10	18	10.1	0.02	10	

The wave conditions at both facilities were generated using Froude number scaling with a length scale of $l_s = 1 : 100$. All the tests presented in this study correspond to short-crested sea states based upon the standard JONSWAP frequency spectrum defined by Hasselmann et al. (1973) as:

$$S_{\eta\eta}(f) = \frac{\alpha g^2}{(2\pi)^4 f^5} \exp\left[-\frac{5}{4}\left(\frac{f_p}{f}\right)^4\right] \gamma^{G(f)}, \tag{1}$$

where $G(f)$ is the JONSWAP peak enhancement function

$$G(f) = \exp\left[\frac{-(f - f_p)^2}{2\sigma^2 f_p^2}\right] \tag{2}$$

with $\gamma = 2.5$, α the energy scale factor, f_p the spectral peak frequency, $g = 9.81 \text{ ms}^{-2}$ the gravitational acceleration, and $\sigma = 0.07$ for $f \leqslant f_p$ and $\sigma = 0.09$ for $f > f_p$. The two-dimensional wave spectrum, $E(f; \theta)$, is then given by:

$$E(f; \theta) = S_{\eta\eta}(f)D(f; \theta), \tag{3}$$

where a wrapped-normal directional spreading function has been introduced as:

$$D(f; \theta) = \frac{A}{\sigma_\theta} \exp\left(-\frac{\theta^2}{2\sigma_\theta^2}\right). \tag{4}$$

In Eq. (4), θ is the angle of propagation of each wave harmonic relative to the mean wave direction, σ_θ is the standard deviation of the frequency-independent directional spreading and A is a normalising factor. The present tests are characterised by directional spreads of $\sigma_\theta = 10°$ and $\sigma_\theta = 20°$, which correspond to commonly encountered sea-state conditions in finite water depths.

Table 1 summarises the key characteristics (at full scale) of the sea-states considered in the ICL wave basin. In total, wave spectra with 3 peak periods, $T_p = [12 \text{ s}, 14 \text{ s} \text{ and } 16 \text{ s}]$, are simulated for a range of sea-state steepnesses and 2 directional spreads ($\sigma_\theta = [10°, 20°]$). By defining the deep-water steepness as:

$$S_p = \frac{2\pi H_s}{g T_p^2}, \tag{5}$$

sea-states ranging from near-linear to extreme are derived using a step of $\Delta S_p = 0.01$. Therefore, each test case is defined using the triad $(H_s, T_p, \sigma_\theta)$; where the significant wave height, H_s, is calculated using the spectral definition:

$$H_s = 4\sqrt{\int_0^\infty S_{\eta\eta}(f) \, df}. \tag{6}$$

For each test case, 20 random simulations (or seeds), each of 3-hour duration, have been conducted using an extension of the Random Directional Method (Latheef et al., 2017) described in Karmpadakis
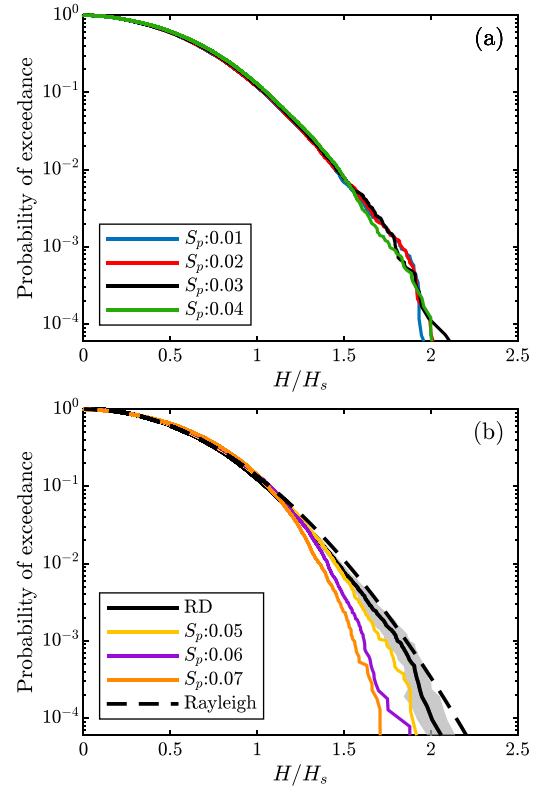

Fig. 1. Normalised wave height distributions, H/H_s, corresponding to the IA experimental cases with $k_p d = 1.53$ and $\sigma_\theta = 10°$. (a) Data correspond to the lowest sea-steepness cases [$S_p = 0.01 - 0.04$]. (b) The representative distribution (RD) and its 95% confidence intervals (CIs) for the data in sub-plot (a) are compared against the largest steepness cases [$S_p = 0.05 - 0.07$] and the Rayleigh distribution.

and Swan (2020). In effect, each realisation with the same T_p and σ_θ is characterised with the same set of (initial) random phases for all steepness cases. As such, direct comparisons between individual waves in sea-states of increasing steepness become possible. Moreover, given the substantial number of observed individual waves (16,000–20,000) in each sea-state, the application of this method increases confidence in the description of the largest waves.

Finally, it should be noted that the full matrix of test cases was simulated in the ICL wave basin, while a subset of these was generated using different water depths [$d = 40, 50$ and 60 m] in the QUB wave basin. These are summarised in Table 2. Additional details of the experimental setup can be found in Karmpadakis et al. (2019) and Karmpadakis and Swan (2020).

The field observations used in this study constitute a subset of the large database of wave records analysed by Karmpadakis et al. (2020). These have all been recorded, using high sampling rates, by wave radars mounted on offshore platforms in the southern North Sea. As a whole, the measurements have been conducted in 10 different locations with water depths in the range 7.7 m < d < 45 m. In total the dataset comprises of approximately 900,000 20-minute sea-states covering a wide range of intermediate and shallow water depths.

The analysis of the raw field measurements involves the following steps. First, strict quality control (QC) procedures are invoked to remove erroneous measurements from the time-series. This is conducted in accordance with Christou and Ewans (2014). The QC'd records are then partitioned into 20-minute samples which define individual sea-states. Subsequently, each of these sea-states is analysed using standard time-frequency techniques to obtain met-ocean parameters (such as H_s and T_p), zero-crossing wave heights (H) and spectral parameters. By selecting small increments of representative met-ocean parameters, the
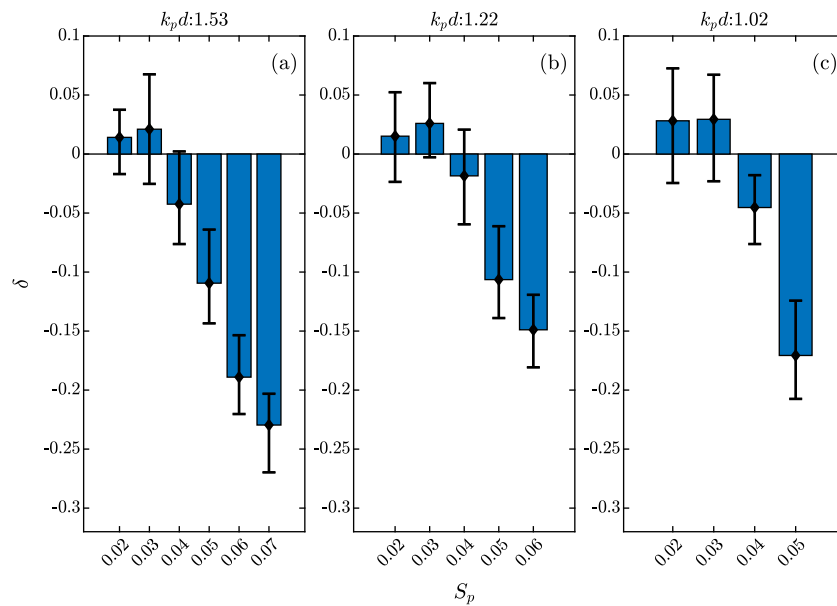
Fig. 2. Bar plots of the difference of normalised wave heights (δ) arising at $Q = 10^{-3}$ recorded in the ICL wave basin (Table 1) for $k_p d =$ (a) 1.53, (b) 1.22 and (c) 1.02. All the data relate to $\sigma_\theta = 10°$ and their 95% CIs have been added for reference.

data related to individual sea-states are grouped (or binned) to yield larger datasets with similar characteristics. This method of stratified sampling is explained in detail in Karmpadakis et al. (2020).

4. Physical insights

The physical processes that define the wave height distributions are investigated through targeted comparisons across the core experimental results outlined in Table 1. Specifically, the effects of nonlinearity, directionality, effective water depth and spectral bandwidth are analysed below.

4.1. Nonlinearity

It is well established that nonlinear effects arising at a second-order of wave steepness do not alter the distribution of wave heights. The questions that arise are: (1) whether higher-order nonlinear effects lead to increases in wave heights for steep sea-states, and, (2) what is the role of wave breaking in such cases.

To address these questions, sea-states with the same effective water depth ($k_p d$) but increasing (deep-water) steepness (S_p) are compared. To facilitate these comparisons, the measured wave heights arising in all realisations of a sea-state are normalised by their corresponding significant wave height (H_s), amalgamated and re-ordered to yield the measured wave height distribution. Such comparisons are shown on Fig. 1. In this and subsequent figures, the x-axis represents the normalised wave heights while the logarithmic y-axis shows the probability of exceedance [$Q = \Pr(h > H)$].

The data shown on Fig. 1 correspond to the IA cases, observed in the ICL wave basin, with $k_p d = 1.53$ and $\sigma_\theta = 10°$. The wave height distributions arising in the 4 lowest steepness sea-states ($S_p = 0.01 - 0.04$) are given on Fig. 1(a). It is clear that the difference between these distributions is very small. Considering that some of these sea-states are steep, this result suggests that either there is no significant increase in wave height statistics owing to higher-order nonlinear wave interactions [$> O(a^2 k^2)$] or any potential nonlinear increase in the large wave heights is counterbalanced by dissipation due to (limited) wave breaking.

In fact, data relating to these sea-states are shown to converge to the same representative distribution (RD) on Fig. 1(b). The latter has been

obtained by averaging the wave height distributions on Fig. 1(a) and, subsequently, calculating the corresponding 95% confidence interval using 10,000 bootstrap samples (Efron, 1987). Having superimposed the wave height distributions for the remaining 3 (highest) steepness cases ($S_p = 0.05 - 0.07$), it can be seen that the largest wave heights in these steeper cases begin to diverge from the representative distribution of the lower steepness cases. This is apparent in the progressive drop in the tail of the distributions as sea-state steepness increases. At the same time, smaller wave heights ($Q > 10^{-1}$) appear to slightly increase. This behaviour is related to the effects of wave breaking (both spilling and overturning), which was observed throughout these simulations. The explanation lies in two parts. First, wave energy dissipation leads to a decrease of the wave heights and a redistribution of the broken wave heights towards larger probabilities of exceedance. Second, with significant wave breaking (sometimes referred to as wave breaking saturation) H_s will reduce. As a result, the smaller unbroken waves will be larger than predicted because they are associated with a sea-state that was both higher and steeper (in the absence of wave breaking). Further discussion of these effects is given in Karmpadakis et al. (2019). To some extent, this justifies the approach of using split probability models (e.g. Battjes and Groenendijk, 2000) to describe the lower and higher probability range. Finally, the Rayleigh distribution, given by:

$$Q(h > H) = \exp\left[-2\left(\frac{H}{H_s}\right)^2\right] \tag{7}$$

is added for reference. The Rayleigh distribution is shown to over-predict the RD, as well as its upper 95% confidence bound. The increase in sea-state steepness leads to progressively larger deviations from the Rayleigh distribution. While the former observation is related to finite spectral bandwidth, the latter is linked to wave breaking. In both cases, the Rayleigh model is shown to lack the essential physical input to describe the measured data.

It is insightful to extend the analysis to the full matrix of test cases. To perform this, a representative probability of exceedance, $Q = 10^{-3}$, is selected and its corresponding wave height, $H_{0.001}$, calculated. After normalising this wave height with the significant wave height of the sea-state, a measure of discrepancy is defined as:

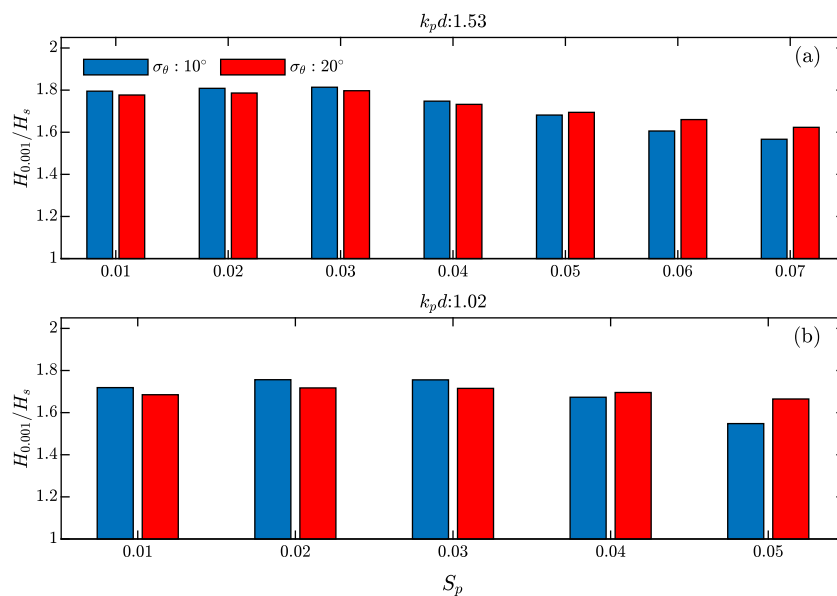$$\delta = \frac{H_{0.001}^i}{H_s^i} - \frac{H_{0.001}^1}{H_s^1}, \tag{8}$$

Fig. 3. Normalised wave heights $H_{0.001}/H_s$ arising at a probability $Q = 10^{-3}$ comparing sea-states with different directional spreading σ_θ across cases with increasing sea-state steepness. Sub-plot (a) concerns the IA tests ($k_p d = 1.53$) while sub-plot (b) includes the IC tests ($k_p d = 1.02$).

where the superscript i indicates the steepness case. In effect, δ illustrates the differences in the wave height arising at increasing sea-state steepnesses relative to the (near-linear) case of $S_p = 0.01$. These would be positive when nonlinear interactions (second-order and above) are important and negative when wave breaking is dominant.

Fig. 2 presents the δ values, along with 95% CIs, for all the experimental cases recorded in the ICL wave basin with $\sigma_\theta = 10°$. When examining these results, a consistent pattern arises across all effective water depths. The normalised wave heights initially exhibit a small increase for $S_p = 0.02 - 0.03$. This is followed by much sharper reductions for larger S_p values. While the initial increases are observed for all effective water depths, their magnitude is limited to below 3% and they lie well within the 95% confidence bounds. This confirms the previous finding that nonlinear wave–wave interactions do not have a profound influence on large wave heights. In contrast, the degree of energy dissipation is shown to progressively increase with increasing sea-state steepness. Indeed, this can reach levels larger than 15%. Undoubtedly, this indicates the increased importance of wave breaking in the steepest sea-states as well as the need to accurately account for it. It is worth noting the selected probability level ($Q = 10^{-3}$) has been chosen because of its broad employment in design calculations and the fact that it represents the general behaviour of the tail of the distribution (where the largest waves appear).

Taking all of these data together, the main finding regarding the impact of nonlinearity on the observed wave height distributions is that it does not significantly affect the shape of the distribution until wave breaking begins to have a significant effect. The transition from one state to the other occurs for H_s/d values of approximately $0.2 - 0.3$; the latter limit being observed in both laboratory measurements and field data (Karmpadakis et al., 2020).

4.2. Directionality

In this section, the effects of directionality or short-crestedness on the measured wave height distribution are investigated by comparing sea-states with different directional spreads, but all other parameters held constant. The role of directionality is addressed on Fig. 3. This concerns data from (a) the IA experimental cases with $k_p d = 1.53$, and (b) the IC experimental cases with $k_p d = 1.02$. The effect of directionality is captured by examining the variation in the normalised

wave heights $H_{0.001}/H_s$ (for $Q = 10^{-3}$) between sea-states with $\sigma_\theta = 10°$ and $\sigma_\theta = 20°$.

Before proceeding with comparisons between different degrees of directional spreading, it is worth examining the evolution of $H_{0.001}/H_s$ with increasing sea-state steepness when considering one directional spreading in isolation. As indicated in Section 4.1, the results corresponding to $\sigma_\theta = 10°$ show a small initial increase in wave height followed by large reductions for the steepest sea-states. Fig. 3 shows that similar changes arise in sea-states with $\sigma_\theta = 20°$, irrespective of the effective water depth ($k_p d = 1.53$ on Fig. 3(a) and $k_p d = 1.02$ on Fig. 3(b)). As such, the qualitative behaviour of large wave heights within sea-states of increasing steepness does not change with increases in the directional spreading.

However, comparisons between wave heights with the same sea-state steepness reveal subtle differences when the directional spreading is increased. In Fig. 3(a), wave heights arising in sea-states with $\sigma_\theta = 10°$ are (marginally) larger than their counterparts with $\sigma_\theta = 20°$ for $S_p = 0.01 - 0.04$. For $S_p = 0.05 - 0.07$ this trend is reversed with results corresponding to wider directional spreading being larger than the less spread cases. Interestingly, this reversal coincides with the initiation of large reductions in wave heights due to wave breaking. The same behaviour is observed in the data presented in Fig. 3(b); the only difference being that the transition in order occurs between $S_p = 0.03$ and $S_p = 0.04$. As such, these findings apply to a wider range of effective water depths, including the remaining cases in Table 1 which are omitted for brevity.

Overall, the increase in directionality is shown to reduce the largest wave heights, provided there is no significant wave breaking. In contrast, for a sea-state that contains a large number of breaking waves, larger directional spreads result in larger waves. In considering these effects, it should be noted that the changes in the magnitude of the normalised wave heights with directionality do not exceed 2% for moderate steepnesses and 6% for the steepest case.

The explanation for these observations lies in two parts. First, an increase in the directionality leads to a reduction in the individual wave steepness, even in a linear sense. As such, although the wave heights are not critically dependent on the sea-state steepness nonlinear effects will be affected by directionality. More significantly, with the occurrence of wave breaking critically dependent on individual wave steepness, the limiting effects of breaking will inevitably be dependent upon the underlying directional spread. Increased directionality leads to reduced steepness, less breaking and hence larger wave heights.
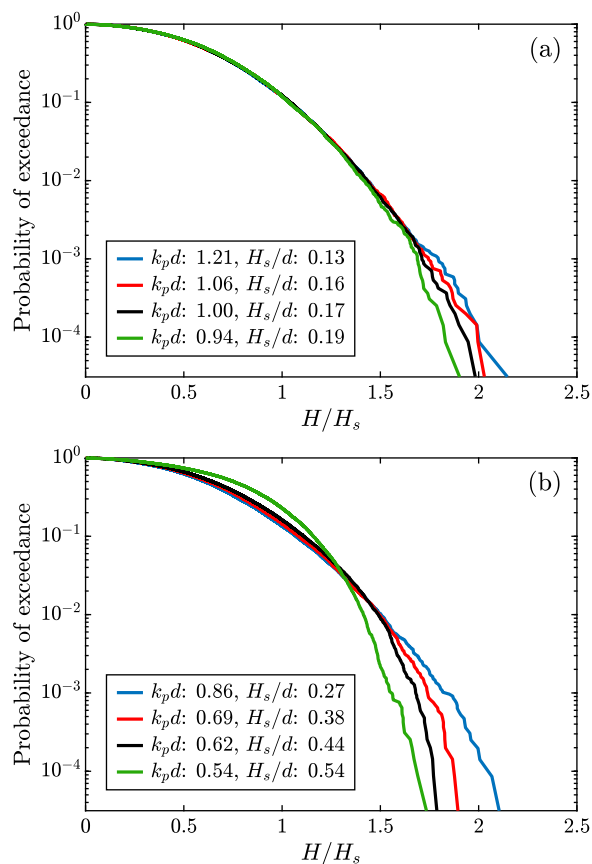
Fig. 4. Normalised wave height distributions, H/H_s, showing the influence of effective water depth as waves propagate over the sloping bed in the QUB wave basin. Comparisons are provided between data arising in sea-states of varying H_s/d and k_pd with respect to cases: (a) Q1B2-10 (offshore depth: $d = 60$ m) and (b) Q3B2-10 (offshore depth: $d = 40$ m).

4.3. Effective water depth

It is well known that a reduction in the effective water depth leads to enhanced nonlinear wave effects, notably sharper crests and flatter troughs. This section employs three alternative approaches to investigate the influence of effective water depth on the distribution of wave heights.

The first approach concerns comparisons between normalised wave height distributions arising from measurements at different wave gauge locations over the sloping bed in the QUB wave basin. In adopting this method, the changes in the wave height distribution can be captured as waves propagate towards shallower water depths. Fig. 4 presents the normalised wave height distributions, H/H_s, recorded at 4 locations over a 1:48 slope. These data relate to sea-states Q1B2-10 and Q3B2-10 with upstream water depths of 60 m and 40 m respectively; both having $H_s = 6.1$ m, $T_p = 14$ s and $\sigma_\theta = 10°$. It is also worth noting that as waves propagate towards the absorbing beach both k_pd and H_s/d change simultaneously; the changes being indicated in the figure legends.

In examining Fig. 4(a), it is shown that the bulk of the wave height distributions are in close agreement for all k_pd values. At the same time, small variations in the tail of the distributions are attributed to wave breaking. In contrast, Fig. 4(b) shows significant changes in the shape of the normalised distributions as the water depth reduces. Considering the high H_s/d values characterising these data, this result is not surprising. Indeed, it merely suggests that the effects of wave breaking increase in importance and, thereby, affect the shape of the wave height distributions. Keeping in mind that the same input spectra

were used in the generation of these two sea-states, a combination of the two figures provides a summary of the evolution of the wave height distribution. This evolution relates to the propagation of waves over the sloping bed and covers the effective water depth range $0.54 < k_pd < 1.21$.

It is clear that the data presented in Fig. 4 will be influenced by the presence of the slope. Any effects of wave shoaling, nonlinear wave–wave interactions, wave breaking and bottom dissipation would either be not present or different if a flat bed was considered. To minimise their influence, the data included in these comparisons correspond to locations which were at most a few wavelengths upstream the toe of the slope. As a result, they did not exhibit significant spectral evolution. Whilst (Katsardi et al., 2013) indicate that mild sloping beaches have a less pronounced effect on the wave height distribution, the effect of the bathymetry cannot be completely discarded. As such, the main purpose of this approach is to indicate the progressive change in the shape of the wave height distribution appropriate to data recorded over both sloping and flat beds.

Concerns regarding the importance of energy dissipation and wave-slope interactions can be removed by applying the second method of investigation. Following this approach, the same sea-states (defined in terms of H_s, T_p and σ_θ) were generated in different water depths. In practice, following the completion of a set of test cases, the water level in the QUB wave basin was reduced and exactly the same simulations repeated; all of the data being recorded over the flat bed section of the wave basin. In detail, Fig. 5(a) shows comparisons between the normalised wave heights, H/H_s, for cases Q1B2-10 and Q3B2-10 with water depths (at full scale) of $d = 60$ m and $d = 40$ m respectively. Both sea-states have the same moderate steepness ($S_p = 0.02$) and lie below the breaking transition, $H_s/d < 0.15$; the effective water depths being $k_pd = 1.42$ and 1.04, respectively. Comparisons between the wave height distributions show that these cases are in close agreement. Similarly, Fig. 5(b) concerns the same cases but generated with a directional spread of $\sigma_\theta = 20°$ Once again, the wave height distributions are in close agreement. These examples are representative of a wide range of moderate incident conditions. They indicate that in such cases, changes in the effective water depth do not significantly affect the wave height distribution regardless of the directional spread of the sea-state. Finally, Fig. 5(c) presents measurements corresponding to the same effective water depths, $\sigma_\theta = 10°$ but increased sea-state steepness $S_p = 0.03$. In this case, the data relating to the lowest k_pd exhibit reductions in the largest wave heights. The values of H_s/d in each case (Q1B3-10, Q3B3-10) were 0.15 and 0.23, respectively. This places the shallowest sea-state into the transition zone where the effects of wave breaking begin to become important. It, therefore, follows that the reduction in the tail of the wave height distribution can be attributed to wave breaking.

Considering data with moderate steepnesses and low H_s/d values [Fig. 5(a)–(b)], it is clear that the reduction in the effective water depth does not induce significant changes in the normalised wave height distributions. However, for sea-states with more extensive wave breaking (characterised by larger H_s/d values) changes will occur. For sea-states with the same H_s and T_p values, shallower locations will be more affected by wave breaking and their wave height distribution will change accordingly.

Further evidence of this mechanism is provided by the third set of comparisons. Once again, all of the data relate to measurements over the flat bed. In this case, the water depth (d) and sea-state steepness (S_p) have been kept constant, but different spectral peak periods, T_p, have been considered. With a change in T_p, the significant wave height, H_s, must also change to keep S_p (Eq. (5)) constant; the role of reduced water depth being expressed through the variation in k_pd. Using this approach a wide range of effective water depths can be investigated.

Fig. 6(a) shows comparisons of this type involving test cases Q3A2-10, Q3B2-10, Q3C2-10 and Q3D2-10 with a steepness of $S_p = 0.02$. All sea-states were generated in a water depth of $d = 40$ m; their k_pd
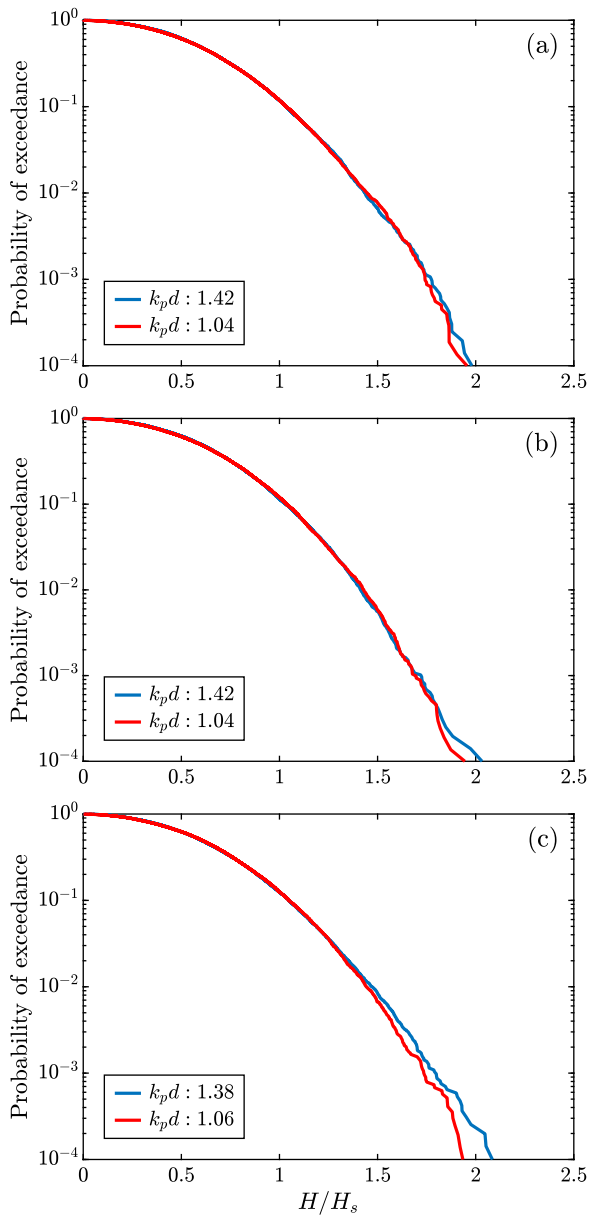
Fig. 5. Normalised wave height, H/H_s, distributions recorded in the QUB wave basin. Each sub-plot concerns sea-states with the same H_s, T_p and σ_θ generated in two water depths ($d = 60$ m and $d = 40$ m). The data correspond to pairs of cases: (a) Q1B2-10/Q3B2-10, (b) Q1B2-20/Q3B2-20 and (c) Q1B3-10/Q3B3-10.

values ranging between 1.3 and 0.78 (full details being given in the figure legend). In comparing these cases, it can be seen that all the wave height distributions exhibit a similar form. However, some minor differences appear to arise in the tail of the distributions. More specifically, sea-states with larger effective water depth are characterised by smaller (normalised) wave heights (H/H_s). Nonetheless, it can be seen that these differences are both small in magnitude and confined to the tail of the distribution ($Q < 10^{-3}$). These results suggest that reduced effective water depth does not have a significant impact on the wave height distribution, as long as there is little or no wave breaking. In this sense, they are in agreement with the observations made using the previous approaches.

In contrast, steeper sea-states ($S_p = 0.04$) generated in the ICL wave basin with H_s/d values in the transition zone provide clear evidence of how the relative water depth progressively drives the change of the
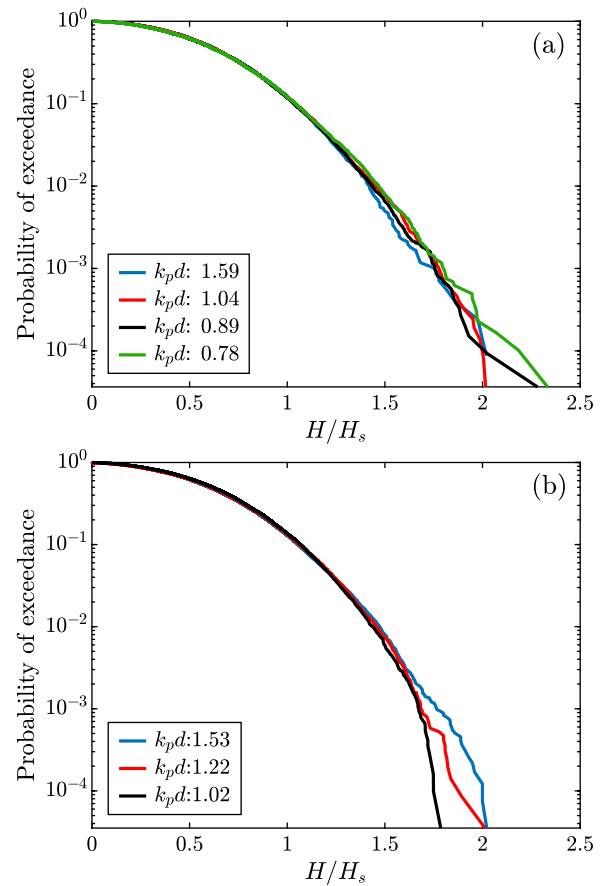

Fig. 6. Normalised wave height distributions showing comparisons between cases with the same S_p but different k_pd. The data correspond to: (a) test cases Q3A2-10, Q3B2-10, Q3C2-10 and Q3D2-10 in the QUB wave basin and (b) IA4-10, IB4-10 and IC4-10 in the ICL wave basin.

wave height distribution. This is illustrated in Fig. 6(b) using cases IA4-10, IB4-10 and IC4-10 with corresponding k_pd values of 1.53, 1.22 and 1.02. Based upon these data, it is clear that as k_pd reduces, the sea-states become increasingly saturated with breaking waves and the tail of the distribution substantially reduces.

In combining the results from the three approaches adopted herein, it has been shown that the main effect of reducing the effective water depth of a sea-state is related to the onset of wave breaking. Having identified that the transition to sea-states with significant breaking is initiated for H_s/d values in the range of 0.2–0.3, the shapes of the wave height distributions are similar for all water depths below this transition. In contrast, for higher H_s/d values the largest waves in a sea-state are progressively reduced.

4.4. Spectral bandwidth

The importance of finite spectral bandwidth in deep-water wave height statistics has historically received considerable attention (Longuet-Higgins, 1980; Tayfun, 1981; Forristall, 1984; Boccotti, 1989). This section employs an additional set of experiments to investigate its effect in shallower water depths.

Sea-states with different spectral shapes were generated in the QUB wave basin under the shallowest water depth configuration ($d = 40$ m). These would represent sea-states at different stages of development (fetch and wind speeds) as described in Holthuijsen (2010). Specifically, Gaussian spectra with varying standard deviations, σ_f, were utilised to incorporate a broad range of spectral bandwidths. Using the JONSWAP sea-states with $S_p = (0.02, 0.03)$ and $\sigma_\theta = 10°$ as the
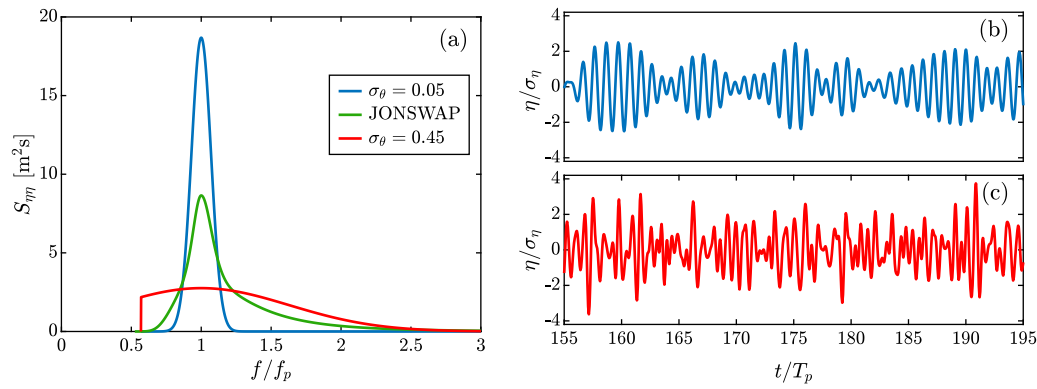
Fig. 7. (a) Gaussian and JONSWAP frequency spectra used as input for an investigation of the effects of spectral bandwidth and time-histories of the surface elevations, $\eta(t)$, illustrating the differences between (b) narrow-banded and (c) broad-banded Gaussian spectra.

Table 3
Additional laboratory test cases undertaken in the QUB wave basin ($d = 40\,\text{m}$) to investigate the role of spectral bandwidth. All the test cases are characterised by $T_p = 14\,\text{s}$ ($k_p d = 1.05$) and $\sigma_\theta = 10°$.

Sea-state	H_s [m]	S_p [–]	σ_f [Hz]
G2S05	6.1	0.02	0.05
G2S45	6.1	0.02	0.45
G3S05	9.1	0.03	0.05
G3S45	9.1	0.03	0.45

basis for the test cases, additional sea-states with two different standard deviations were simulated. These are characterised by $\sigma_f = 0.05$ to represent the most narrow-banded conditions, and $\sigma_f = 0.45$ for the most broad-banded. Full details of these sea-states are given on Table 3. Fig. 7(a) shows the different spectral shapes arising from this approach. In generating these sea-states, the Gaussian spectra have been truncated and scaled to yield the target H_s and T_p values. The truncation of the (broad-banded) spectra in the low-frequency range was required due to the mechanical limitations of the wave paddles. For each test case, 10 random realisations were conducted. Indicatively, Fig. 7 also presents surface elevation records normalised by their standard deviation, η/σ_η, arising in the narrowest [7(b)] and broadest [7(c)] spectral bandwidths. These have been obtained from numerical (linear random wave theory) simulations using test cases from Table 3 (G2S05, G2S45). It is clear that the increase in spectral bandwidth leads to a rapid de-correlation between the wave crests and troughs. Building upon this, wave height distributions arising in broad-banded conditions are expected to be smaller than those arising in the equivalent narrow-banded sea-states.

To confirm this effect, Fig. 8(a) concerns numerically simulated data based upon linear random wave theory and the experimental input spectra. Within this figure, the normalised wave heights, H/H_s, arising from 10 random simulations of a sea-state with $S_p = 0.02$, $k_p d = 1.05$ and $\sigma_\theta = 10°$ have been compared. The comparisons include a narrow-banded spectrum with $\sigma_f = 0.05$ (G2S05-10) and a broad-banded spectrum with $\sigma_f = 0.45$ (G2S45-10). The wave heights corresponding to a JONSWAP spectrum with a peak enhancement factor $\gamma = 2.5$ (Q3B2-10) and the Rayleigh distribution have also been added. It can be seen that the wave heights obtained from the narrow-banded spectrum are significantly larger than the ones from the broad-banded spectrum and very close to the predictions of the Rayleigh distribution. The data relating to the JONSWAP spectrum lie between the two Gaussian spectra, but are closer to the broad-banded results. At this point, it is worth noting that the JONSWAP spectrum utilised in this comparison is equivalent to a Gaussian spectrum with $\sigma_f = 0.25$ in terms of spectral bandwidth.

Fig. 8(b) shows the same sea-states generated experimentally in the QUB wave basin. The generated data are in close agreement with linear simulations. This is expected given the (moderate) steepness and

confirms that the effect of increasing spectral bandwidth is to reduce the wave heights. In this respect, it is also verified that bandwidth effects arise at a first-order of wave steepness.

Fig. 8(c) presents cases with the same $k_p d$ as previously, but larger sea-steepness, $S_p = 0.03$. This increase does not appear to have a profound effect on any of the wave height distributions. The only exception concerns a small reduction in the wave height corresponding to the smallest probabilities. This latter effect is predominantly caused by wave breaking, as indicated in previous sections. While all these data correspond to the offshore flat bed region of the QUB wave basin, it is insightful to consider data with smaller effective water depths. This is addressed in Fig. 8(d); data from cases with $S_p = 0.03$ being recorded in a shallower water depth and described by $H_s/d = 0.46$ and $k_p d = 0.69$. It can be seen that the wave height distributions converge to the same shape; the differences between different spectral bandwidths have almost entirely diminished. In seeking to explain these results, it is clear that the observed behaviour is primarily driven by excessive, depth-induced, wave breaking and the subsequent energy dissipation. As such, differences in the (offshore) spectral bandwidth seem to have limited influence in saturated sea-states. In interpreting this result, it should be kept in mind that nonlinear wave evolution and wave breaking will naturally lead to a broadening of the offshore frequency spectrum.

Taken together, the results presented in this section indicate the major importance of spectral bandwidth for sea-states with low H_s/d values and the significance of wave breaking in steeper sea-states. In drawing these conclusions it is worth noting that the use of truncated Gaussian spectra is intended to provide the effects of finite spectral bandwidth and, in no way, implies that such spectra represent realistic storm conditions. Nevertheless, they provide effective upper and lower bounds within which realistic wave heights are expected to occur.

5. New wave height model

Recently, Karmpadakis et al. (2020) showed that across the large variety of existing wave height models, there is not one (individual) model that provides equally accurate predictions across a wide range of water depths. Whilst suggestions have been made regarding the best performing distributions under different water depth regimes, there is a need for a single wave height model that would be applicable under a broad range of incident conditions. The development of such a model is presented in this section.

To achieve this, the physical insights provided thus far have been taken into account. Specifically, the effects of nonlinearity, reduced effective water depth and spectral bandwidth are explicitly incorporated into the new model. However, given the small effect of directionality, the proposed model is not parametrised for different degrees of directional spreading. Instead, it is calibrated using the large database of short-crested ($\sigma_\theta = 10°$) experimental measurements in the ICL and

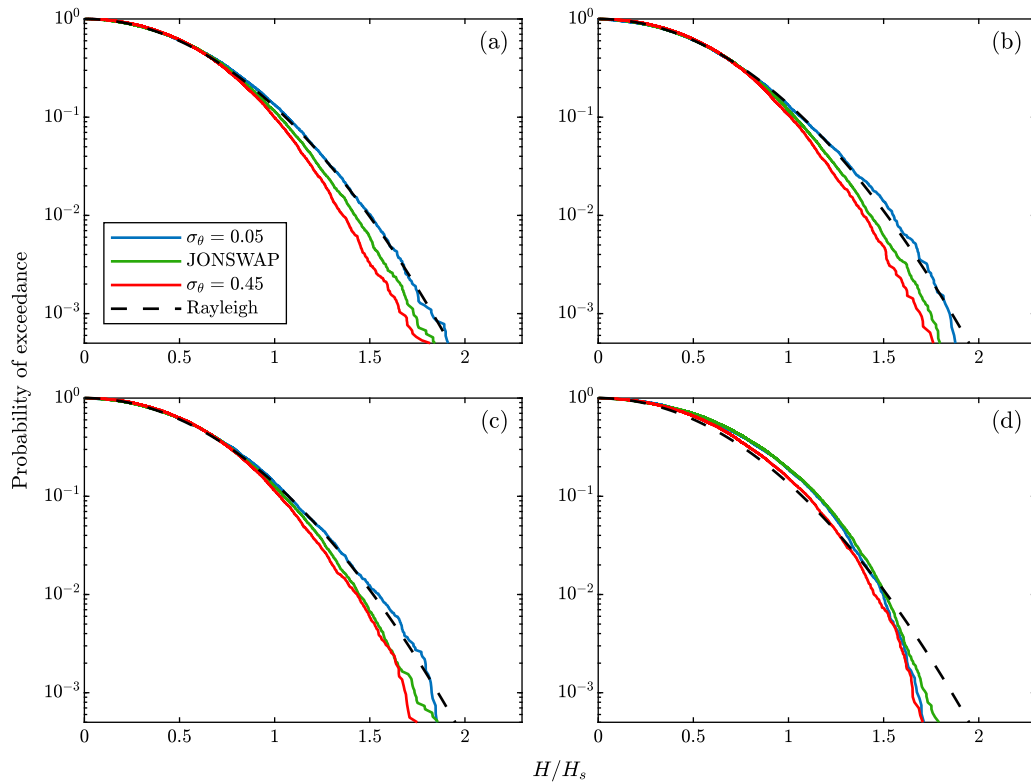**Fig. 8.** Normalised wave height, H/H_s, distributions showing the effects of spectral bandwidth. The input conditions relate to Gaussian frequency spectra with $\sigma_f = 0.05$ and $\sigma_f = 0.45$ as well as a JONSWAP spectrum; all with $T_p = 14\,\text{s}$ and $\sigma_\theta = 10°$. The data in sub-plots (a) are numerically simulated using linear random wave theory, while sub-plot (b) relates to experimental data; both characterised by $S_p = 0.02$ (G2S05, G2S05 and Q3B2-10). Sub-plots (c) and (d) relate to case Q3B3-10 ($S_p = 0.03$) and correspond to (c) $k_p d = 1.05$ and (d) $k_p d = 0.69$. The Rayleigh distribution has been added as reference.

QUB wave basins. Moreover, it is subsequently validated independently against the field data analysed by Karmpadakis et al. (2020). The wave height model is intended to be easy to implement, valid across a range of water depths and predictive. The latter implies that the model can be applied using sea-state parameters that are readily available from standard hindcast models or field measurements.

In deriving a functional form for the model, the option of employing a two-part distribution was considered. This approach was adopted by Battjes and Groenendijk (2000) and Wu et al. (2016) to describe the behaviour of the smallest and largest wave heights separately. However, this would necessarily require the introduction of additional empirical parameters in the model formulation. This, in turn, has the potential to make the model less robust and more dependent on the specific dataset used for its calibration. To avoid such issues, a two-parameter Weibull form was selected. The basis of the model builds upon the Glukhovskiy (1966) distribution which was shown to be in reasonable agreement with a broad range of field data (Karmpadakis et al., 2020).

Taking these points into consideration, the functional form of the wave height model is given by:

$$Q = \exp\left[-A\left(\frac{H}{H_{\text{rms}}}\right)^K\right], \tag{9}$$

where H_{rms} is the root-mean-square wave height, A is the scale parameter and K the shape parameter. The moment generating function of this distribution is given by (Klopman, 1996):

$$M_n = H_{rms}^n A^{-n/K} \Gamma\left(\frac{n}{K} + 1\right), \tag{10}$$

where M_n is the nth-order moment and Γ is the gamma function.

First, the exponent, K, of the distribution is defined; the function of this parameter being to control the shape of the distribution. Building upon the physical insights provided in Section 4, the main requirement

for this shape parameter is to reduce the tail of the (probability of exceedance) distribution for sea-states with substantial wave breaking. Given that these saturated sea-states are characterised by large H_s/d values, the shape parameter K should increase with increasing H_s/d. At the same time, it has been shown that for moderate sea-states, changes in the nonlinearity do not have a significant impact on the shape of the distribution. This implies that for low H_s/d values the shape parameter should vary by only a small amount. More importantly, the success of bandwidth-limited models (Tayfun and Fedele, 2007), suggests that the Rayleigh exponent of $K = 2$ can accurately describe the wave height distribution. Combining these requirements, the behaviour of K should be to increase for the steepest and shallowest sea-states, while asymptotically tending to the Rayleigh exponent in deep water. Furthermore, the transition in the magnitude of the shape parameter should be smooth rather than occurring at a single point; the latter being defined by the transition zone ($0.2 < H_s/d < 0.3$) described in the previous sections.

Having defined the criteria appropriate to the description of the shape parameter, the experimental data were used to fit empirical Weibull distributions. An important aspect of this process relates to the method of fitting. It was found that traditional methods (such as the method of moments or maximum likelihood estimation) did not perform well in the steepest sea-states. This comes as no surprise as these sea-states are characterised by significant wave breaking. In such cases, the distribution of wave heights can no longer be described by a single Weibull model. In other words, the wave height distribution comprises of two populations: one containing "broken" waves and another with smaller waves, as explained by Battjes and Groenendijk (2000). To overcome this problem, a tail preserving method was used to approximate the measured wave height distributions. Effectively, this means that the Weibull fits were forced to have the best possible representation in the tail of the distribution for each sea-state. This was

Table 4
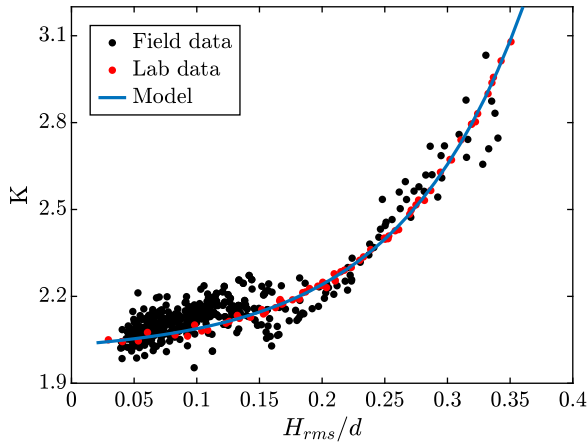Empirical coefficients defining the shape parameter K [Eq. (11)].

Parameter	a	b	c
Model	0.032	10.02	2

Fig. 9. Parametrisation of the shape parameter, K, of the proposed wave height distribution.

Fig. 10. Assessment of the approximation for $H_{\mathrm{rms}}/\sqrt{m_0}$ by the deep-water [Eq. (12)], Battjes–Groenendijk [Eq. (13)] and Mendez [Eq. (14)] formulas using the field database. The x-axis shows the saturation range $\sqrt{m_0}/d$.

achieved by conditioning the wave heights on $H/H_s \gtrsim 0.5$. In effect, this approach acts to prioritise the description of the largest waves, which can be easily justified considering that the primary engineering interest lies in the behaviour of the biggest waves.

Once the shape parameters arising from these fits were obtained, an equation for K could be derived using least-squares error minimisation. The best fit to the experimental data was given by a function of the form:

$$K = a \exp\left(b \frac{H_{\mathrm{rms}}}{d} \right) + c, \tag{11}$$

where a, b and c are empirical coefficients defined in Table 4.

Fig. 9 compares the empirically fitted shape parameters, K, with the predictions of Eq. (11). It is clear that the proposed approximation provides a good description of the experimental data, on which the fit was based. In addition, the corresponding shape parameters arising in the field measurements have been added in the same figure. It can be seen that the proposed approximation shows generally good agreement across all data. However, the results relating to the field data are characterised by larger variability. These discrepancies can be explained by the sensitivity in the estimation of the shape parameters in cases with fewer data and the wide range of met-ocean conditions encountered in the field. In any case, the general trend in the behaviour of K with varying H_{rms}/d appears to be well described. Since the field data were not employed in the calibration of the model, no effort was made to improve the original (experimental) fit.

Taken together, these results show that the shape parameter of the wave height distribution tends asymptotically to $K = 2$ for deeper water; the latter being indicated by the constant c in Eq. (11). Simultaneously, K grows exponentially for sea-states with large H_{rms}/d values; the scale and rate of change being provided by a and b in Eq. (11).

The value of H_{rms} used thus far is not a readily available parameter; its calculation depending on the analysis of the measured wave heights. According to linear wave theory in deep water:

$$H_{\mathrm{rms}}/H_s = \frac{\sqrt{2}}{2}, \tag{12}$$

for a narrow-banded process. However, this ratio is subject to change when nonlinear wave–wave interactions, finite spectral bandwidth and wave breaking are considered. Both Battjes and Groenendijk (2000) and Mendez et al. (2004) have approximated this ratio using data
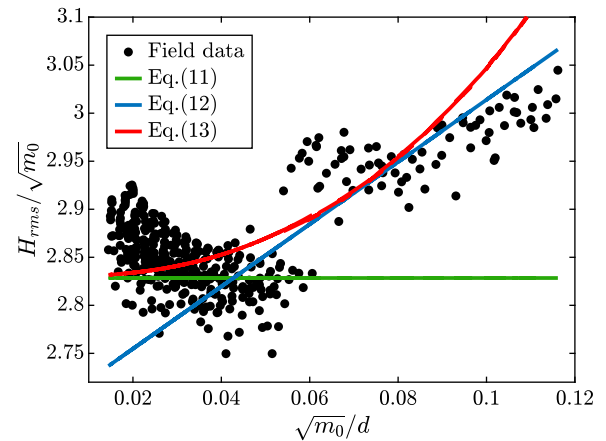
generated on sloping bathymetries. These approximations primarily incorporate increases in H_{rms}/H_s following the shoreward propagation of waves and are given by:

$$H_{\mathrm{rms}} = \left(2.69 + 3.24 \frac{\sqrt{m_0}}{d} \right) \sqrt{m_0} \quad \text{and} \tag{13}$$

$$H_{\mathrm{rms}} = \sqrt{8m_0} + 1.15\kappa \sqrt{m_0}, \tag{14}$$

respectively. In the above equations, the zeroth spectral moment is denoted by m_0, while κ is a parameter dependent on the Iribarren number (Equation (15) in Mendez et al. (2004)). Fig. 10 provides a comparison between these equations and available field data. The x-axis defines a wave breaking saturation parameter, $\sqrt{m_0}/d$, and the y-axis is the normalised $H_{\mathrm{rms}}/\sqrt{m_0}$. It can be seen that while the positive gradient for the shallowest data is qualitatively captured, the approximation for more moderate (shallow water) sea-states ($\sqrt{m_o}/d \approx 0.06$) and deeper water is not good. This is, in part, the reason why these models have been found to over-estimate wave heights in intermediate water depths and flat bed bathymetries (Mai et al., 2011; Caires and Van Gent, 2012; Karmpadakis et al., 2020).

In incorporating this observation, alongside the notable influence of finite spectral bandwidth on the wave height distribution, the proposed model employs an alternative parametrisation for H_{rms}. In effect, an effort is made to explain the variability observed in the data of Fig. 10 by accounting for spectral bandwidth. As such, the effect of finite bandwidth is introduced directly into the estimation of H_{rms}, following the findings of Rice (1944). This is achieved by adopting the notions underpinning the Boccotti (1989) distribution and other bandwidth limited deep-water distributions.

Starting from the spectral density function, $S_{\eta\eta}(f)$, the normalised autocorrelation function of the spectrum is calculated by:

$$r(\tau) = \frac{\int_0^\infty S_{\eta\eta}(f) \cos(2\pi f \tau)\, df}{\int_0^\infty S_{\eta\eta}(f)\, df}, \tag{15}$$

where τ represents a time lag. In defining T^* as the time lag in which the first minimum of the autocorrelation function, $r(\tau)$, appears, the non-dimensional parameter ρ can be defined as:

$$\rho = r(T^*). \tag{16}$$

This is used to express the degree of de-correlation between wave crests and troughs (Naess, 1985; Boccotti, 1989) using:
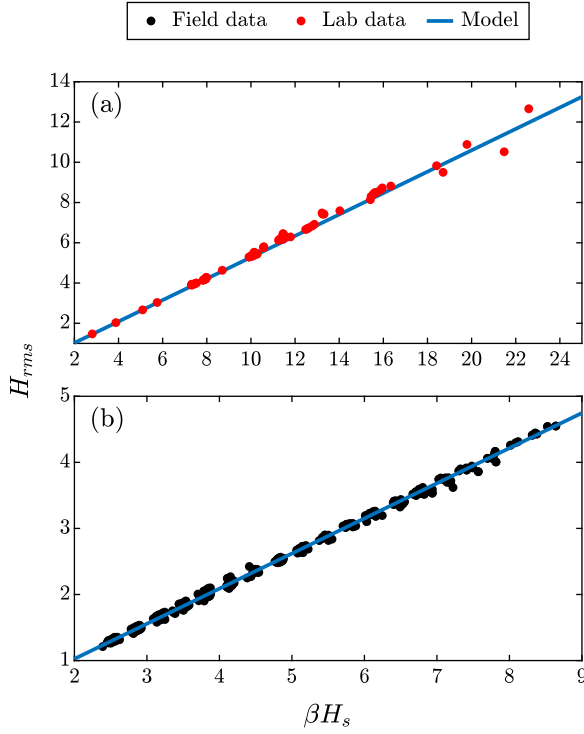
$$\beta = \sqrt{1 - \rho}. \tag{17}$$

Fig. 11. Parametrisation of H_{rms} with respect to βH_s. The quality of the fit of Eq. (18) is shown with respect to (a) laboratory data and (b) field data.

In the present wave height distribution, a linear regression model is established using the laboratory measurements to parametrise H_{rms}. This is given by:

$$H_{rms} = 0.5316\beta H_s - 0.03776. \tag{18}$$

and is justified by the linear relationship between H_{rms} and βH_s shown on Fig. 11. The data presented on this figure is entirely consistent with those shown on Fig. 10: the red dots denoting the laboratory data used to define the parametric fit of Eq. (18) and the black dots the field data showing the appropriateness of the chosen fit. Moreover, all of the field data presented on Fig. 10 are included on Fig. 11; the chosen parametrisation leading to a much reduced scatter.

For completeness, it should be noted that the spectral density function required for these calculations can be obtained using any of the standard formulae (e.g. Hasselmann et al., 1973; Bouws et al., 1985) or measured data if available. With respect to JONSWAP spectra, the following formula proposed by DNV (2010) can be used to infer an appropriate peak enhancement factor, γ:

$$
\begin{aligned}
\gamma &= 1 & & 5 \leq T_p/\sqrt{H_s} \\
\gamma &= \exp\left(5.75 - 1.15\frac{T_p}{\sqrt{H_s}}\right) & & 3.6 < T_p/\sqrt{H_s} < 5 \\
\gamma &= 5 & & T_p/\sqrt{H_s} \leq 3.6.
\end{aligned} \tag{19}
$$

Having defined the shape parameter of the distribution and provided an approximation for the normalising factor (H_{rms}), the last step in the derivation of the new model involves the calculation of the scale parameter A. This is obtained analytically by equating the second moment of the distribution (M_2) with $\sqrt{H_{rms}}$ and is given by:

$$A = \left[\Gamma\left(\frac{2}{K}+1\right)\right]^{K/2}, \tag{20}$$

where Γ is the gamma function, $\Gamma(x) = \int_0^\infty t^{x-1}e^{-t}dt$ and K the shape parameter defined above. This approach ensures that the proposed model represents a consistent probability function.

6. Comparisons to available field data

The model, as described above, is fully defined using Equations [(9), (11), (18) and (20)]. It depends only on the commonly available sea-state parameters H_s, T_p and d and the selection of an appropriate spectral shape, such as the JONSWAP spectrum in Eq. (1). In assessing the accuracy of the proposed wave height model, the stratified sampling ("data binning") approach mentioned in Section 3 was applied.

First, the distributions of wave heights arising in single data bins, defined as (H_s, T_p) bands, are examined. As such, Fig. 12 compares the measured (normalised) wave heights, H/H_s, to the proposed wave height model. The comparisons relate to 4 distinctively different cases with $H_s/d \in [0.07, 0.4]$ and $k_p d \in [0.44, 3.93]$. It is clear that this parameter range covers both a wide variety of deep-to-shallow water depths and moderate-to-steep sea-states. In addition, three wave height models commonly applied in engineering practice have been superimposed in each sub-plot. These refer to the Rayleigh, Boccotti and Battjes–Groenendijk models; their functional forms being provided in Appendix for reference.

Considering each case in turn, Fig. 12(a) presents data arising in relatively deep water sea-states of moderate steepness. It can be seen that the present model and the Boccotti distribution are in good mutual agreement, describing the measurements with high accuracy. In contrast, both the Rayleigh and Battjes–Groenendijk models over-estimate the largest wave heights. A similar pattern arises in Fig. 12(b), in which steeper and shallower sea-states are considered. Apart from a small departure in the tail of the distribution, both the present and Boccotti models are in good agreement with the data. In considering these comparisons, it is important to note the characteristic change in the gradient of the Battjes–Groenendijk model at $Q = 10^{-3}$. This indicates the transition to a wave regime in which the largest wave heights are dominated by wave breaking. Despite providing an improvement over the Rayleigh distribution, the predictions of the Battjes–Groenendijk model diverge from the measured data.

Fig. 12(c) and (d) present comparisons to much shallower and steeper sea-states. In both cases, the proposed wave height model shows very good agreement with the field data. In contrast, the Boccotti model cannot capture the sharp drop in the tail of the distribution due to wave breaking. The Battjes–Groenendijk model appears to qualitatively capture the occurrence of substantial wave breaking. However, it consistently underestimates the magnitude of the largest waves. Considering these results, the present wave height model is shown to provide a good representation of the field data over a broad range of effective water depths. Indeed, it approximates the successful model of Boccotti (1989) in deeper water and accurately incorporates the effects of wave breaking in shallower/steeper sea-states.

In an effort to further illustrate the success of the proposed model, a second method of assessment involves the identification of the best performing distribution amongst a longer list of available models. To achieve this, the 4 models presented above are supplemented by the: Forristall (1978), Naess (1985), Klopman (1996), van Vledder (1991), Mendez et al. (2004) and Wu et al. (2016) models; their functional forms being summarised in Appendix. In partitioning the (H_s, T_p) parameter space within each measurement location into bins of the same size (0.5 m, 1 s), the measured wave heights are compared to the predictions of each model. To quantify the divergence between predictions and measurements, the following RMS error (ε) was defined:

$$\varepsilon = \sqrt{\frac{1}{N}\sum_{i=p}^{N}\left(\frac{H^i_{measured}}{H^i_{model}}-1\right)^2}, \tag{21}$$

where N is the number of zero-crossing wave heights, $H_{measured}$ and H_{model} are the measured and predicted wave heights. In each calculation the summation starts from the pth observation corresponding to the percentile under investigation, and extends towards the smallest
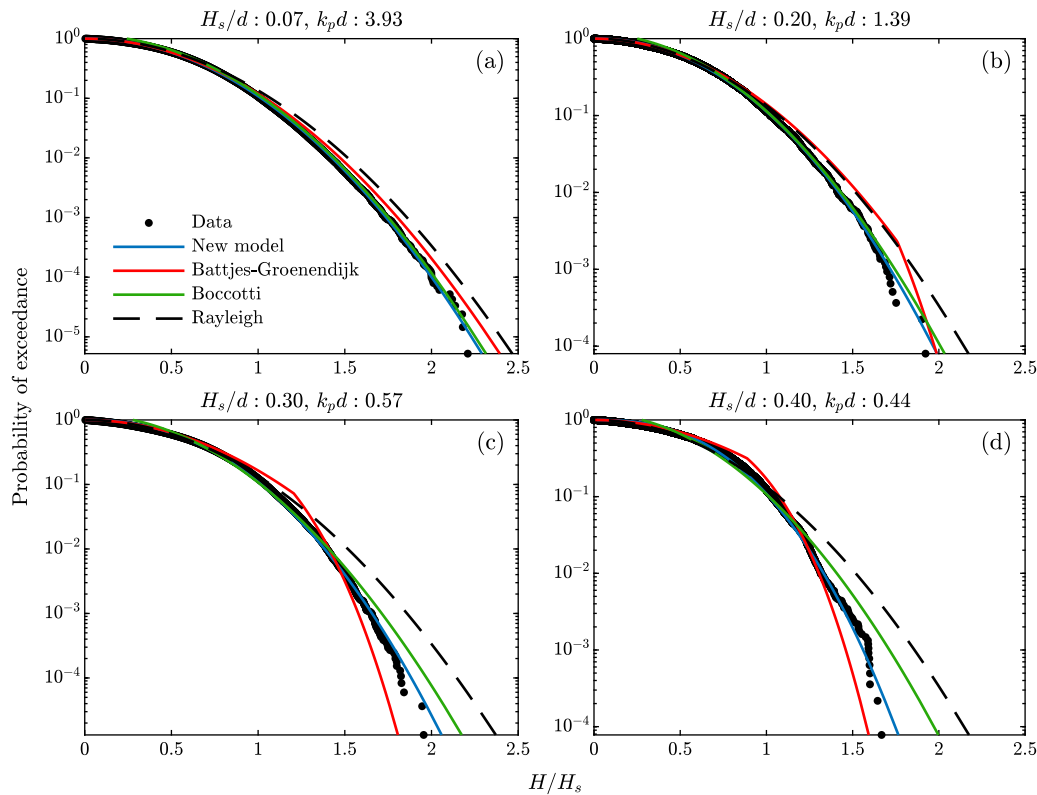
Fig. 12. Normalised wave height distributions, H/H_s, showing comparisons between the present, Battjes–Groenendijk, Boccotti and Rayleigh models. The H_s/d and $k_p d$ values corresponding to each group of sea-states are noted in the titles, while the data were recorded at (a) $d = 35$ m, (b) $d = 25$ m and [(c),(d)] $d = 7.7$ m.

probability of exceedance. Percentiles corresponding to P_{20} (20%) and P_1 (1%) have been selected to reflect the behaviour in the main body and tail of the distributions respectively. Once the error associated with each model was calculated, the data points in each bin were coloured to reflect the model that best matches the measurements.

The methodology described above is the same as the one employed by Karmpadakis et al. (2020) in their assessment of existing wave height models using the same field dataset. Their Figs. 5 and 7 provide the best fitting distributions in the full dataset and individual measuring locations. Their key finding is that for low H_s/d values the Boccotti model performs best for the majority of cases, while for increasing H_s/d values a variety of models (Klopman, van Vledder, Battjes–Groenendijk and Mendez) are more appropriate. As a whole, no model was found to provide the best fit with a consistent level of accuracy.

Fig. 13 extends these results by including the present wave height model in the assessment. Specifically, Fig. 13(a) relates to the P_{20} percentile, while Fig. 13(b) to the P_1 percentile; both incorporating all the available data. The best-fitting maps are expressed in the non-dimensional ($k_p d$, H_s/d) parameter space and clearly show that the new wave height model produces consistently accurate predictions. This refers to both the bulk (P_{20}) and the tail P_1 of the distributions. While there are other models that also provide the best fit in specific data bins, the overarching trend is that the newly proposed model has the best overall performance.

The compilation of results in Fig. 13(a)–(b) unavoidably involves the combination of data with the same met-ocean parameters from different measuring locations. This could potentially lead to complications if wildly different results arise for the same conditions at different locations. Karmpadakis et al. (2020) have shown that this is not the case for the present dataset by examining the results from individual locations in isolation. To confirm that this is indeed the case, Fig. 13(c)–(d) present results relating to the P_1 percentile from platforms with $d = 27.4$ m and $d = 7.7$ m, respectively. These have been selected as representative examples of deep-to-intermediate and

intermediate-to-shallow regimes; their combined H_s/d range covering $H_s/d \in [0.06, 0.65]$ with a transition between them at $H_s/d \approx 0.2$. In examining these results, it can be seen that the proposed wave height model provides the best fit for the vast majority of the sea-states under consideration. Importantly, the significant variability in the best fit model observed in Karmpadakis et al. (2020) (see their Fig. 7) is drastically reduced. This is particularly relevant to cases with large H_s/d in which the earlier predictions of best performing models were very heterogeneous.

Taken together, the model presented herein is shown to accurately describe the wave height distributions arising in a very wide range of effective water depths and incident wave conditions. More importantly, the proposed wave height model has been designed to incorporate the effects of wave breaking and spectral bandwidth; both having been shown to significantly affect the wave height distributions. At the same time, the proposed model is characterised by a simple functional form, which could easily be recalibrated or extended as additional datasets become available. Considering the work conducted herein, the presently proposed calibration coefficients have been derived on the basis of laboratory measurements. In applying these, the model has been shown to give accurate (and independent) predictions to the available field data.

7. Concluding remarks

The statistical distribution of zero-crossing wave heights in intermediate and shallow water depths over flat bed bathymetries has been investigated. Using laboratory data it has been shown that nonlinearity and reduced effective water depth have no significant impact on the wave height distribution, provided wave breaking is not dominant (low H_s/d values). In contrast, for higher H_s/d values, both effects lead to a significant reduction of the largest wave heights and a characteristic change in the wave height distribution. The latter effect is initiated in
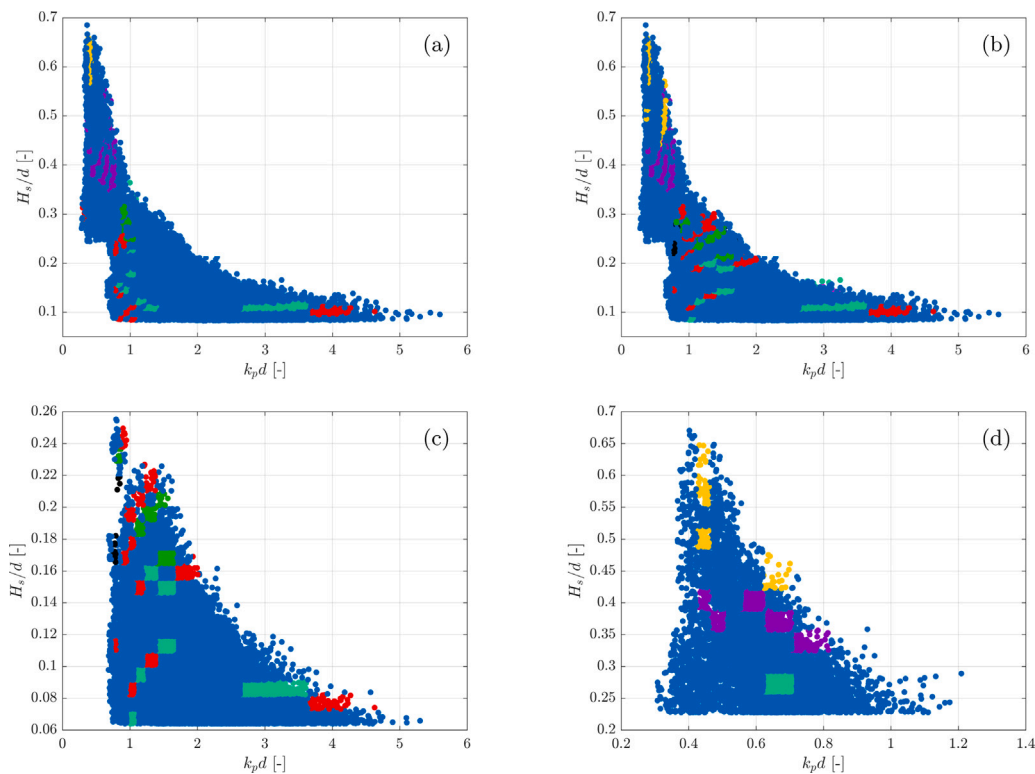
Fig. 13. Maps in the $(k_p d, H_s/d)$ parameter space indicating the best fitting distribution for the (a) P_{20} and (b)–(d) P_1 percentiles. Sub-plots (a)–(b) present results from the full field dataset, while sub-plots (c)–(d) relate to locations with $d = 27.4$ m and $d = 7.7$ m, respectively. The distributions are: Proposed model [●], Forristall [●], Klopman [●], van Vledder [●], Battjes–Groenendijk [●], Mendez [●], Wu [●], Boccotti [●], Naess [●].

the tail of the distribution and progressively affects the smaller wave heights.

It has also been demonstrated that directionality acts to reduce the largest wave heights within sea-states of moderate steepness. In contrast, in sea-states that contain a large number of breaking waves, larger directional spreads result in larger wave heights. However, the magnitude of the changes induced by directionality are generally small.

Changes in the spectral bandwidth have also been shown to have a significant impact on the wave height distribution, primarily for larger effective water depths. More specifically, broad-banded sea-states are characterised by reduced wave heights. With respect to smaller effective water depths, spectral bandwidth appears to be less important once extensive wave breaking occurs.

Moreover, a new wave height model has been proposed. This has been derived on the basis of laboratory measurements and incorporates the physical insights identified herein. It incorporates explicitly the effects of nonlinearity, reduced effective water depth and finite spectral bandwidth arising in short-crested sea-states. The proposed wave height model has been independently validated using the field database of Karmpadakis et al. (2020). In undertaking this validation, it has become clear that the new model can provide significant improvements over existing models and is applicable to a wide range of water depths and sea-state parameters.

CRediT authorship contribution statement

I. Karmpadakis: Conceptualization, Formal analysis, Methodology, Investigation, Visualization, Writing – original draft, Writing – review & editing. **C. Swan:** Conceptualization, Supervision, Funding acquisition, Writing – review & editing. **M. Christou:** Conceptualization, Supervision, Funding acquisition, Writing – review & editing.

Declaration of competing interest

The authors declare that they have no known competing financial interests or personal relationships that could have appeared to influence the work reported in this paper.

Appendix. Existing wave height distributions

The functional forms of wave height distributions used in the present study are provided as follows. More details about these models can be found in the respective publication and the recent review by Karmpadakis et al. (2020).

(a) Forristall distribution (Forristall, 1978)

$$Q(H) = \exp\left[-\frac{1}{\beta}\left(\frac{H}{\sigma_\eta}\right)^\alpha\right], \tag{A.1}$$

where H denotes the wave heights, σ_η the standard deviation of the free surface elevation, $\alpha = 2.126$ and $\beta = 8.42$.

(b) Naess distribution (Naess, 1985)

$$Q(H) = \exp\left[-\frac{1}{4(1-r(T^*))}\left(\frac{H}{\sigma_\eta}\right)^2\right]. \tag{A.2}$$

where $r(\tau)$ is normalised autocorrelation function of the surface elevation and T^* is the abscissa of its first minimum defined in Eq. (16).

(c) Boccotti distribution (Boccotti, 1989)

$$Q(H) = \frac{1 + \ddot{r}(T^*)}{\sqrt{2\ddot{r}(T^*)(1 - r(T^*))}} \exp\left[-\frac{1}{4(1 - r(T^*))}\left(\frac{H}{\sigma_\eta}\right)^2\right],$$ (A.3)

where T^* is, again, the abscissa of the first minimum of the autocorrelation function of the surface elevation, $r(\tau)$, and the double over dot denotes the second time derivative: $\ddot{r}(t) = \partial^2 r/\partial t^2$.

(d) Klopman distribution (Klopman, 1996)

$$Q(H) = \exp\left[-A\left(\frac{H}{H_{\text{rms}}}\right)^K\right],$$ (A.4)

where

$$A = \left[\Gamma\left(\frac{2}{K} + 1\right)\right]^{K/2}$$ (A.5)

and $K = \dfrac{2}{1 - \beta H_{\text{rms}}/d}$. (A.6)

The root-mean-square wave height is obtained as $H_{\text{rms}} = H_s/\sqrt{2}$, Γ is the gamma function defined by $\Gamma(x) = \int_0^\infty t^{x-1}e^{-t}dt$ and $\beta = 0.7$ is an empirical coefficient.

(e) van Vledder distribution (van Vledder, 1991)

$$Q(H) = \exp\left[-A\left(\frac{H}{H_m}\right)^K\right],$$ (A.7)

coupled with an iterative scheme defined by:

$$K^i = \frac{2}{1 - H_m^i/d},$$ (A.8)

$$H_m^{i+1} = H_{\text{rms}} \frac{\Gamma\left(\frac{1}{K^i} + 1\right)}{\sqrt{\Gamma\left(\frac{2}{K^i} + 1\right)}},$$ (A.9)

where i is the counter. For the first iteration, $(i = 1)$ (van Vledder, 1991) uses H_m^1 obtained from the Rayleigh distribution, while the scale parameter A is given in Eq. (A.5).

(f) Battjes–Groenendijk distribution (Battjes and Groenendijk, 2000)

$$Q(H) = \begin{cases} \exp\left[-\left(\frac{H}{H_1}\right)^{K_1}\right] & \text{for } H \leq H_{tr} \\ \exp\left[-\left(\frac{H}{H_2}\right)^{K_2}\right] & \text{for } H > H_{tr}. \end{cases}$$ (A.10)

The empirical coefficients are defined by

$$K_1 = 2, \qquad K_2 = 3.6,$$ (A.11)

$$H_{tr} = (0.35 + 5.8\tan\alpha)d$$ (A.12)

and $$H_{\text{rms}} = \left(2.69 + 3.24\frac{\sigma_\eta}{d}\right)\sigma_\eta,$$ (A.13)

where $\tan\alpha$ is the (average) bed slope in the direction of dominant wave propagation (shore-normal). The normalising wave heights H_1 and H_2 can be obtained from Table 2 of the (Battjes and Groenendijk, 2000) paper.

(g) Mendez distribution (Mendez et al., 2004)

$$Q(H) = \exp\left[-\phi^2(\kappa)\left(\frac{\xi}{1 - \kappa\xi}\right)^2\right], \qquad \text{for } 0 \leq \xi < 1/\kappa,$$ (A.14)

where $\xi = H/H_{\text{rms}}$. The scale parameter $\phi(\kappa)$ was defined by Mendez et al. (2004) as

$$\phi(\kappa) = (1 - \kappa^{0.944})^{1.1877},$$ (A.15)

while the empirical coefficient κ is:

$$\kappa = \left(\frac{H_{\text{rms}}}{d}\right)^{2.5}(4.7 - 20.8 Ir + 26.2 Ir^2),$$ (A.16)

where Ir is the Iribarren number defined by

$$Ir = \frac{\tan a}{\sqrt{H_{\text{rms}}/L_1}};$$ (A.17)

L_1 being the deep water wavelength corresponding to the spectral mean period, T_1, such that $L_1 = gT_1^2/2\pi$.

(h) LoWiSh II distribution (Wu et al., 2016)

$$Q(H) = \begin{cases} \exp\left[-\mu\left(\frac{H}{H_s}\right)^k\right] & \text{for } H \leq H_{tr} \\ \exp(-\mu)\left\{1 + \left[1 + \frac{\xi}{\sigma}(H - H_{tr})\right]^{\left(-\frac{1}{\xi}\right)}\right\} & \text{for } H > H_{tr}. \end{cases}$$ (A.18)

where μ and k are respectively the scale and shape parameters of the Weibull part and ξ is the shape parameter of the Generalised Pareto part; all being defined in Wu et al. (2016).

References

Alkhalidi, M.A., Tayfun, M.A., 2013. Generalized Boccotti distribution for nonlinear wave heights. Ocean Eng. 74, 101–106. http://dx.doi.org/10.1016/j.oceaneng.2013.09.014.

Battjes, J.A., Groenendijk, H.W., 2000. Wave height distributions on shallow foreshores. Coast. Eng. 40 (3), 161–182. http://dx.doi.org/10.1016/S0378-3839(00)00007-7.

Boccotti, P., 1989. On mechanics of irregular gravity waves. Atti ASccad. Naz. Lincei A 386 Mem./Cl. Sci. Fis. Mat. Nat. 19 (VIII), 111–170.

Bouws, E., Gunther, H., Rosenthal, W., Vincent, C.L., 1985. Similarity of the wind wave spectrum in finite depth water 1. Spectral form. J. Geophys. Res. 90 (C1), 975–986. http://dx.doi.org/10.1029/JC090iC01p00975.

Caires, S., Van Gent, M.R., 2012. Wave height distribution in constant and finite depths. Coast. Eng. Proc. 1 (33), 15. http://dx.doi.org/10.9753/icce.v33.waves.15.

Casas-Prat, M., Holthuijsen, L.H., 2010. Short-term statistics of waves observed in deep water. J. Geophys. Res. Oceans 115 (9), 1–20. http://dx.doi.org/10.1029/2009JC005742.

Christou, M., Ewans, K., 2014. Field measurements of rogue water waves. J. Phys. Oceanogr. 44 (9), 2317–2335. http://dx.doi.org/10.1175/JPO-D-13-0199.1.

DNV, 2010. DNV-RP-C205 Environmental Conditions and Environmental Loads. Technical Report October, pp. 9–123.

Efron, B., 1987. Better bootstrap confidence intervals. J. Amer. Statist. Assoc. 82 (397), 171–185. http://dx.doi.org/10.1080/01621459.1987.10478410.

Fedele, F., Arena, F., 2005. Weakly nonlinear statistics of high random waves. Phys. Fluids 17 (2), 1–10. http://dx.doi.org/10.1063/1.1831311.

Fedele, F., Brennan, J., Ponce De León, S., Dudley, J., Dias, F., 2016. Real world ocean rogue waves explained without the modulational instability. Sci. Rep. 6 (May), 1–11. http://dx.doi.org/10.1038/srep27715.

Fedele, F., Herterich, J., Tayfun, A., Dias, F., 2019. Large nearshore storm waves off the Irish coast. Sci. Rep. 9 (1), 15406. http://dx.doi.org/10.1038/s41598-019-51706-8.

Forristall, G.Z., 1978. On the statistical distribution of wave heights in a storm. J. Geophys. Res. 83 (C5), 2353. http://dx.doi.org/10.1029/JC083iC05p02353.

Forristall, G.Z., 1984. The distribution of measured and simulated wave heights as a function of spectral shape. J. Geophys. Res. 89 (C6), 10547. http://dx.doi.org/10.1029/JC089iC06p10547.

Glukhovskiy, B., 1966. Investigation of sea wind waves (in Russian). In: Leningrad, Gidrometeoizdat (Reference Obtained from Bouws, E. 1979: Spectra of Extreme Wave Conditions in the Southern North Sea Considering the Influence of Water Depth. Proc. of Sea Climatology Conference, Paris: 51-71).

Goda, Y., 2010. Random Seas and Design of Maritime Structures. In: Advanced Series on Ocean Engineering, vol. 33, World Scientific Publishing Company, pp. 1–732. http://dx.doi.org/10.1142/7425.

Hasselmann, K., Barnett, T.P., Bouws, E., Carlson, H., Cartwright, D.E., Enke, K., Ewing, J.A., Gienapp, H., Hasselmann, D.E., Kruseman, P., Meerburg, A., Muller, P., Olbers, D.J., Richter, K., Sell, W., Walden, H., 1973. Measurements of wind-wave growth and swell decay during the joint north sea wave project (JONSWAP). Ergnzungsheft Dtsch. Hydrogr. Z. R. A(8) (12), 95.

Holthuijsen, L.H., 2010. Waves in Oceanic and Coastal Waters. Cambridge University Press, Cambridge, pp. 1–387. http://dx.doi.org/10.1017/CBO9780511618536.

Karmpadakis, I., Swan, C., 2020. On the average shape of the largest waves in finite water depths. J. Phys. Oceanogr. 50 (4), 1023–1043. http://dx.doi.org/10.1175/JPO-D-19-0165.1.

Karmpadakis, I., Swan, C., Christou, M., 2019. Laboratory investigation of crest height statistics in intermediate water depths. Proc. R. Soc. A 475 (2229), 20190183. http://dx.doi.org/10.1098/rspa.2019.0183.

Karmpadakis, I., Swan, C., Christou, M., 2020. Assessment of wave height distributions using an extensive field database. Coast. Eng. 157, 103630. http://dx.doi.org/10.1016/j.coastaleng.2019.103630.

Katsardi, V., de Lutio, L., Swan, C., 2013. An experimental study of large waves in intermediate and shallow water depths. Part I: Wave height and crest height statistics. Coast. Eng. 73, 43–57. http://dx.doi.org/10.1016/j.coastaleng.2012.09.007.

Klopman, G., 1996. Extreme Wave Heights in Shallow Water. Technical Report Delft Hydraulics Report H2486.

Latheef, M., Swan, C., Spinneken, J., 2017. A laboratory study of nonlinear changes in the directionality of extreme seas. Proc. R. Soc. A 473 (2199), 20160290. http://dx.doi.org/10.1098/rspa.2016.0290.

Longuet-Higgins, M.S., 1952. On the statistical distribution of the heights of sea waves. J. Mar. Res. 11 (3), 245–266.

Longuet-Higgins, M.S., 1980. On the distribution of the heights of sea waves: Some effects of nonlinearity and finite band width. J. Geophys. Res. 85 (C3), 1519. http://dx.doi.org/10.1029/JC085iC03p01519.

Longuet-Higgins, M.S., Stewart, R.W., 1960. Changes in the form of short gravity waves on long waves and tidal currents. J. Fluid Mech. 8 (04), 565. http://dx.doi.org/10.1017/S0022112060000803.

Mai, S., Wilhelmi, J., Barjenbruch, U., 2011. Wave height distributions in shallow waters. Coast. Eng. Proc. 1 (32), waves.63. http://dx.doi.org/10.9753/icce.v32.waves.63.

Van der Meer, J., Allsop, N., Bruce, T., De Rouck, J., Kortenhaus, A., Pullen, T., Schüttrumpf, H., Troch, P., Zanuttigh, B., 2018. Manual on wave overtopping of sea defences and related structures. An overtopping manual largely based on European research, but for worldwide application. Report www.overtopping-manual.com.

Mendez, F.J., Losada, I.J., Medina, R., 2004. Transformation model of wave height distribution on planar beaches. Coast. Eng. 50 (3), 97–115. http://dx.doi.org/10.1016/j.coastaleng.2003.09.005.

Mori, N., Janssen, P.A.E.M., 2006. On kurtosis and occurrence probability of freak waves. J. Phys. Oceanogr. 36 (7), 1471–1483. http://dx.doi.org/10.1175/JPO2922.1.

Naess, A., 1985. On the distribution of crest to trough wave heights. Ocean Eng. 12 (3), 221–234. http://dx.doi.org/10.1016/0029-8018(85)90014-9.

Rice, S.O., 1944. Mathematical analysis of random noise. Bell Labs Tech. J. 23 (3), 282–332.

Sharma, J., Dean, R., 1981. Second-order directional seas and associated wave forces. Soc. Pet. Eng. J. 21 (01), 129–140. http://dx.doi.org/10.2118/8584-PA.

Spinneken, J., Swan, C., 2012. The operation of a 3D wave basin in force control. Ocean Eng. 55, 88–100. http://dx.doi.org/10.1016/j.oceaneng.2012.07.024.

Tayfun, M.A., 1981. Distribution of crest-to-trough wave heights. J. Waterw. Port Coast. Ocean Eng. http://dx.doi.org/10.1061/(ASCE)0733-950X(1990)116:6(686).

Tayfun, M.A., 1990. Distribution of large wave heights. J. Waterw. Port Coast. Ocean Eng. 116, 686–707. http://dx.doi.org/10.1061/(ASCE)0733-950X(1990)116:6(686).

Tayfun, M.A., Fedele, F., 2007. Wave-height distributions and nonlinear effects. Ocean Eng. 34 (11–12), 1631–1649. http://dx.doi.org/10.1016/j.oceaneng.2006.11.006.

van Vledder, 1991. Modification of Glukhovskiy Distribution - Southern North Sea Group Annex 2.

Wu, Y., Randell, D., Christou, M., Ewans, K., Jonathan, P., 2016. On the distribution of wave height in shallow water. Coast. Eng. 111, 39–49. http://dx.doi.org/10.1016/j.coastaleng.2016.01.015.